ACS APPLIED MATERIALS & INTERFACES

www.acsami.org

Research Article

Unraveling the (De)sodiation Mechanisms of $BiFeO_3$ at a High Rate with *Operando* XRD

Anders Brennhagen,* Casper Skautvedt, Carmen Cavallo, David S. Wragg, Alexey Y. Koposov, Anja O. Sjåstad, and Helmer Fjellvåg*

Cite This: *ACS Appl. Mater. Interfaces* 2024, 16, 12428−12436

Read Online

ACCESS | Metrics & More | Article Recommendations | Supporting Information

ABSTRACT: Development of new anode materials for Na-ion batteries strongly depends on a detailed understanding of their cycling mechanism. Due to instrumental limitations, the majority of mechanistic studies focus on *operando* materials' characterization at low cycling rates. In this work, we evaluate and compare the (de)sodiation mechanisms of $BiFeO_3$ in Na-ion batteries at different current densities using *operando* X-ray diffraction (XRD) and *ex situ* X-ray absorption spectroscopy (XAS). $BiFeO_3$ is a conversion-alloying anode material with a high initial sodiation capacity of ∼600 mAh g^{-1}, when cycled at 0.1 A g^{-1}. It does not change its performance or cycling mechanism, except for minor losses in capacity, when the current density is increased to 1 A g^{-1}. In addition, *operando* XRD characterization carried out over multiple cycles shows that the Bi ⇋ NaBi (de)alloying reaction and the oxidation of Bi at the interface with the Na−Fe−O matrix are detrimental for cycling stability. The isolated NaBi ⇋ Na_3Bi reaction is less damaging to the cycling stability of the material.

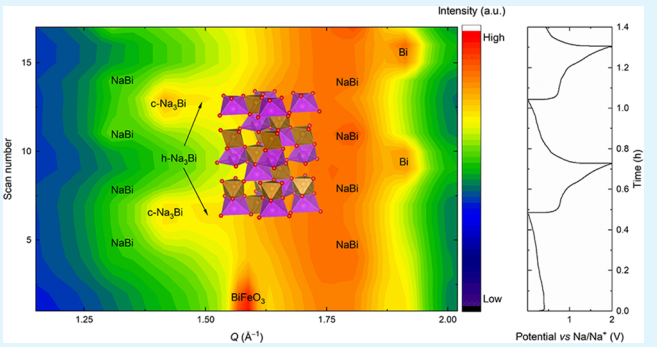

KEYWORDS: *$BiFeO_3$, Na-ion battery, operando XRD, high rate cycling, conversion-alloying materials*

INTRODUCTION

Na-ion batteries (NIBs) have been long viewed as promising alternatives to modern Li-ion batteries (LIBs) due to the high abundance and low cost of Na that can make up for the slightly lower energy densities.[1−3] The application of NIBs is particularly promising in stationary energy storage, where high power is necessary and energy density is less crucial.[4] However, further optimization of NIBs for high power applications requires development of suitable anode materials, whose performance will not suffer at elevated cycling rates. High rate capabilities and ability to achieve a good compromise between high capacity and cycling stability make conversion-alloying materials (CAMs) a promising group of compounds.[5−7] However, their complex cycling and degradation mechanisms, often involving the formation of amorphous phases, make them challenging to develop further. In order to determine the (de)sodiation mechanisms of these materials, it is essential to use *operando* methods, where the structural characterization is performed during electrochemical cycling. This methodology is superior to ex situ characterization due to potential structural relaxation of active materials and risk of side reactions with the environment when the materials are extracted from coin cells during the preparation of ex situ samples.[8−10]

The general cycling mechanism of CAMs at low cycling rates (<150 mA g^{-1}) has been revealed through several studies on LIBs and NIBs with *operando* techniques including X-ray diffraction (XRD), X-ray absorption spectroscopy (XAS), and total scattering computed tomography (TSCT) coupled with ex situ and in situ transmission electron microscopy (TEM).[11−19] These studies have confirmed a conversion reaction during the first sodiation/lithiation, which leads to a phase separation with formation of nanosized particles of the alloying element (Si, Ge, Sn, Sb, Bi) distributed in a Na_xX (X = O, S, Se, Te, P, oxometallates) matrix.[6] During the following cycles, the particles of the alloying element are the main contributors to the capacity. However, there are reports of partially reversible conversion reactions in the binary CAMs[11,18] and electrochemical activity in the transition metal in the matrix of ternary CAMs adding to the capacity.[13,20,21]

Bi metalates are a group of ternary CAMs, which exhibit high capacities as anode materials in NIBs. $BiFeO_3$, $Bi_2(MoO_4)_3$, $BiVO_4$, and Bi_2MoO_6 have previously been explored with primary focus on cycling stability.[14,20,22,23] In

Received: November 17, 2023
Revised: February 9, 2024
Accepted: February 12, 2024
Published: February 27, 2024

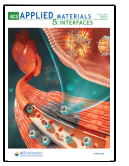

line with the general cycling mechanism of CAMs, Bi metalates undergo an irreversible conversion reaction during the first sodiation to produce Bi nanoparticles embedded in a Na−TM−O (TM = transition metal) matrix. The Bi particles then reversibly transform into Na_3Bi (via NaBi as an intermediate phase) during sodiation.[20,22] There are two known polymorphs of Na_3Bi, hexagonal (h-Na_3Bi) and cubic (c-Na_3Bi). The h-Na_3Bi phase is thermodynamically stable and has been observed to form from microcrystalline NaBi particles, while c-Na_3Bi forms in nanocrystalline NaBi particles (for example, those formed in Bi metallates).[20,24] The buildup of h-Na_3Bi during prolonged cycling of Bi metallates has been linked to particle growth and capacity degradation.[22] Despite significant efforts, we still lack a generalized understanding of the evolution of Na_xBi particles and the Na−TM−O matrix during cycling.[14,20,21]

$BiFeO_3$ is perhaps the most straightforward chemical system among Bi metallates. It has shown reversible (de)sodiation capacities up to 600 mAh g^{-1}, but its cycling stability is limited and the operating mechanism is still disputed.[14,25] Surendran et al. performed *operando* XAS on $BiFeO_3$ and proposed the formation of metallic Fe in addition to Na_2O and an Fe-based oxide during the initial conversion reaction.[14] The same study also showed the presence of Bi−O bonds after the first desodiation, indicating a partial oxidation of Bi metal as was determined by Fourier transformed (FT) extended X-ray absorption fine structure (EXAFS).[14]

The majority of *operando* studies of CAMs have been performed at low current densities and, to the best of our knowledge, there are no *operando* studies addressing the cycling mechanisms of these materials at high cycling rates. This lack of insight is due to the challenges associated with conducting *operando* measurements at high rates: performing reliable electrochemistry in an *operando* cell with an electrode thick enough to obtain a sufficient intensity of X-ray signals. Another limiting factor is the availability of X-ray sources, as synchrotron radiation is needed to obtain high-quality data with high time resolution. In this work, we conducted *operando* XRD measurements, with current densities of 0.1 and 1 A g^{-1}, to elucidate and compare the electrochemical cycling mechanism of $BiFeO_3$ at low and high rates. We also deployed *operando* XRD over 27 (de)sodiation cycles combined with ex situ XAS to gain a further understanding of the interplay between the Na_xBi alloying particles and the Na−Fe−O matrix and their influence on the cycling stability of $BiFeO_3$.

RESULTS AND DISCUSSION

Material and Electrochemical Characterization. Synthesis of phase pure $BiFeO_3$ is recognized as challenging owing to competing ternary phases.[25] After optimization of the reaction conditions, we managed to synthesize $BiFeO_3$ with small amounts of Bi_2O_3 (~12 wt % according to Rietveld refinement) by means of a sol−gel synthetic route (Figure S1, Section S1, SI). The Bi_2O_3 impurities were successfully removed by leaching with nitric acid (Figure S2, SI), but the resulting product showed poor electrochemical performance (Figure S3, SI). Therefore, the unleached product was used for further work.

The electrochemical performance of $BiFeO_3$ was evaluated at different cycling rates with both galvanostatic cycling (GC) and cyclic voltammetry (CV) (Figure S4, Section S2, SI). The initial sodiation capacity of $BiFeO_3$, obtained from GC measurements, was ~600 mAh g^{-1} at 0.1 A g^{-1}, comparable to that of literature reports.[14,25] In addition, fast cycling was undertaken at 1 A g^{-1} where $BiFeO_3$ maintained a reasonable performance. The cycling stability, even at 0.1 A g^{-1}, is nevertheless challenging, and the capacity drops from ~450 mAh g^{-1} to ~130 mAh g^{-1} after 25 cycles.

Elucidation of the Cycling Mechanism at Low and High Rates. Due to experimental limitations, *operando* studies are typically performed under slow cycling conditions, often quite different from the cycling protocols to which electrode materials are subjected in normal use. *Operando* characterization at high cycling rates is rare, despite the fact that understanding of the material's behavior under such conditions is critical for the development of batteries with high power.[26,27] Several CAMs have shown promising electrochemical performance at high rates,[25,28,29] but their cycling mechanisms at these high current densities have not been studied with *operando* methods. To address this problem, we performed *operando* XRD on $BiFeO_3$-based electrodes using synchrotron radiation at BM31 at the European Synchrotron Radiation Facility (ESRF) during electrochemical cycling at 1 A g^{-1} in a half-cell configuration using Na foil as a counter electrode (Figure 1a−c). Surprisingly, $BiFeO_3$ is fully sodiated to Na_3Bi in the first sodiation despite the high current density, confirming that $BiFeO_3$ can maintain the same cycling mechanism and capacity at 1 A g^{-1} as at lower cycling rates.[14,25] Overall, the cycling mechanism was found to be similar to that proposed previously for $BiFeO_3$ and confirmed by *operando* and *post-mortem* studies in other Bi metallates.[14,20,22,25] The minor, but significant difference for $BiFeO_3$ compared to other Bi metallates is the formation of both h-Na_3Bi and c-Na_3Bi phases during the first sodiation, regardless of the current density. This is different from what was shown for $BiVO_4$, $Bi_2(MoO_4)_3$, and Bi_2MoO_6 as they formed only c-Na_3Bi during the first cycles.[20,22] The formation of h-Na_3Bi has been shown to form in microsized NaBi particles, while c-Na_3Bi forms from nanosized NaBi particles.[24] Therefore, the presence of h-Na_3Bi phase after the first sodiation is rather unusual as the presence of h-Na_3Bi has been linked to long-term deactivation of the Bi metallates.[22,24] Furthermore, this suggests that the Bi particles formed during the initial sodiation are slightly larger than those observed for other materials with similar chemistry. This indicates that the size and mobility of the alloying particles could be tuned by customizing the surrounding matrix.

To look for possible variations in the cycling mechanism at different rates, another *operando* measurement was performed with a current density of 0.1 A g^{-1} (Figure 1d−f). As expected, the measurements at 0.1 and 1 A g^{-1} showed the same general cycling mechanism. However, one significant difference was observed: at 1 A g^{-1}, the diffraction peaks for the Na−Bi phases are less defined than those for the 0.1 A g^{-1} measurement. The challenges with performing a high-rate *operando* XRD measurement forced us to find an acceptable compromise between counting statistics and time resolution while maintaining the electrochemical performance, which resulted in less defined diffraction peaks. However, an alternative explanation arises from the lack of time required for the crystallization of the observed phases at high cycling rates, and, therefore, the corresponding peaks do not reach their maximum intensity and sharpness. The limited intensity of the diffraction peaks observed at the 1 A g^{-1} measurement made it difficult to separate the h-Na_3Bi phase from c-Na_3Bi and it was therefore not included in the surface Rietveld refinement.

https://doi.org/10.1021/acsami.3c17296
ACS Appl. Mater. Interfaces 2024, 16, 12428−12436

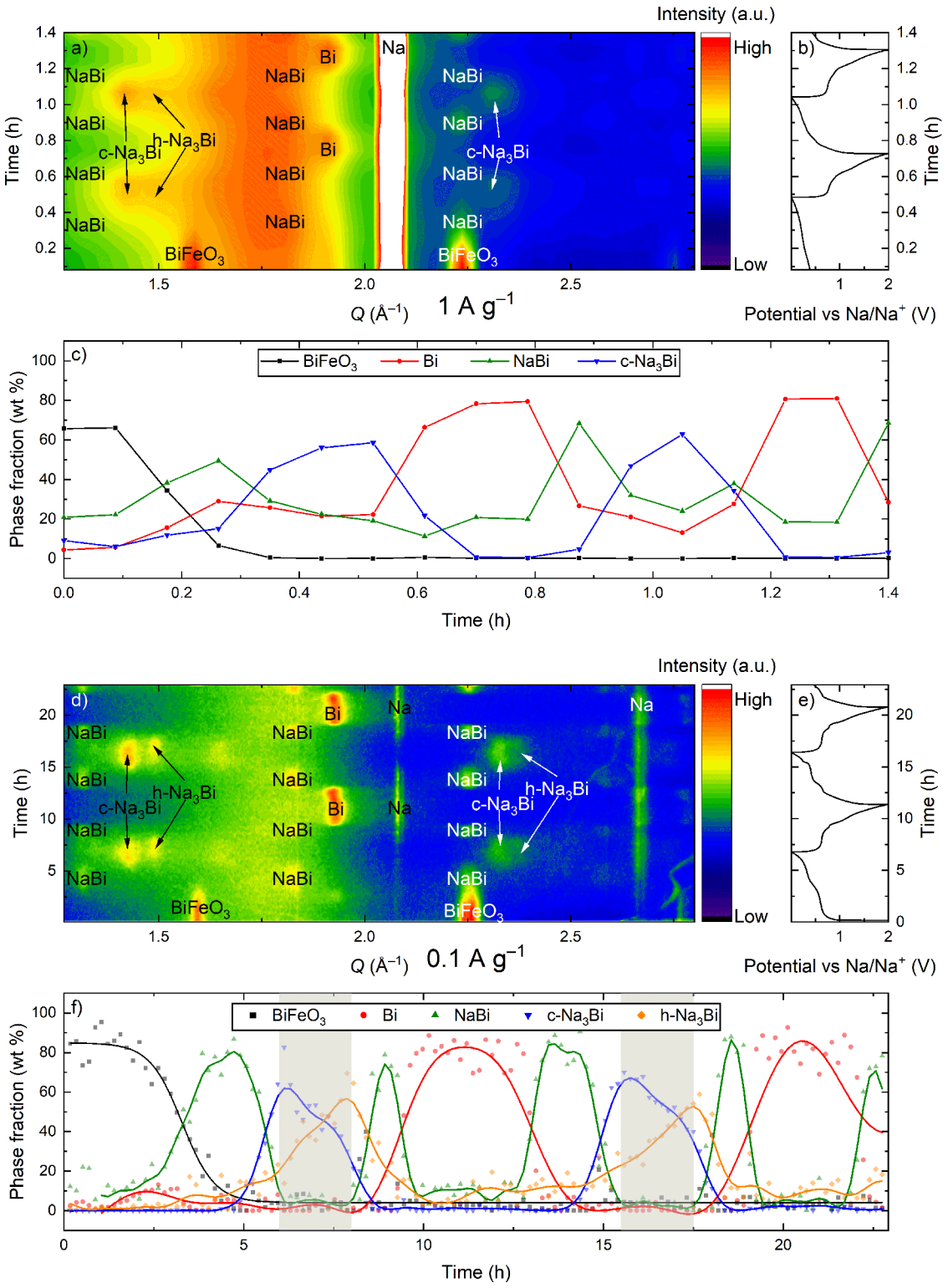

Figure 1. (a) Contour plot derived from the high-rate *operando* XRD measurement of 2 (de)sodiation cycles of $BiFeO_3$, measured with synchrotron radiation at BM31 at ESRF and (b) corresponding (de)sodiation curves measured at 1 A g^{-1}. (c) Phase fractions in wt % retrieved from the surface Rietveld refinement of the diffraction patterns plotted in (a), showing the evolution of the Bi-containing phases as a function of time. The h-Na_3Bi phase is omitted from the surface Rietveld refinement due to limited data quality at a high data collection rate. (d–f) Corresponding graphs for *operando* XRD measurement from the home lab with a current density of 0.1 A g^{-1}. The gray areas in (f) highlight the regions where only c-Na_3Bi and h-Na_3Bi are present.

In addition to the rate comparison, the measurement conducted at 0.1 A g^{-1} provided more detailed insights into the cycling mechanism. Because of the sharper and more intense diffraction peaks, it was easy to distinguish all the different Na_xBi phases and determine the exact moment of their formation. Phase fractions obtained from surface Rietveld

https://doi.org/10.1021/acsami.3c17296
ACS Appl. Mater. Interfaces 2024, 16, 12428−12436

refinement show that the c-Na_3Bi phase forms before h-Na_3Bi (Figure 1f). This is likely because the nucleation of Na_3Bi within the NaBi particles results in the c-Na_3Bi phase, a transformation shown to be more kinetically favorable than that from NaBi to the thermodynamically stable h-Na_3Bi.[24] The formation of h-Na_3Bi starts later and proceeds at the cost of c-Na_3Bi, indicating a transformation from the cubic to the hexagonal phase, possibly when the Na_3Bi crystallites grow to a certain size. Another explanation is that a significant Na deficiency may stabilize in the c-Na_3Bi structure and that h-Na_3Bi forms as full sodiation is achieved: toward the end of sodiation, there is a significant timeslot after the disappearance of NaBi where only the two Na_3Bi phases are present, while the electrochemistry is still active (gray areas in Figure 1f). This transformation cannot be treated as a relaxation process as it is electrochemically driven: ex situ XRD measurements of a sodiated sample conducted 2 weeks after cell disassembly confirmed the presence of c-Na_3Bi and h-Na_3Bi phases in an approximately 7:2 ratio (Figure S5).

Another notable observation is that the time that the NaBi phase is present is significantly shorter during desodiation than sodiation. This could be explained by the formation and dissolution of the SEI layer for each cycle as shown for Bi_2MoO_6 in our previous study.[22] The formation of the SEI during sodiation consumes Na ions and, therefore, contributes to the capacity. This formation prolongs the duration of the sodiation, while the dissolution process during desodiation does not contribute significantly to the capacity. Another possibility is that the reaction paths during desodiation are slightly different from that for sodiation, which has previously been shown for the alloying reactions between Na and P.[30]

Oxidation of Bi and the Nature of the Na−Fe−O Matrix. Most of the works on CAMs have been primarily focused on the electrochemically active materials, while the chemistry of the matrix and its interaction with the active component are still poorly understood. The XRD data described above combined with ex situ XAS measurements provided information on the local structure in the matrix material, the nature of its chemical interaction with the alloying particles, and how they influence each other.

In the desodiated state between ∼10 and 13 h (>1 V), the only detectable XRD peak from the working electrode is the peak corresponding to Bi metal (Figure 1d−f). However, a significant capacity (∼200 mAh g^{-1}) is observed when assessing the contribution above 1 V during the first desodiation (Figure S4c), which suggests that additional chemical transformations other than (de)sodiation of Na_xBi particles take place at this voltage window. The ex situ XAS measurements of the Bi L3 edge confirmed that the oxidation state of Bi in the fully desodiated sample is higher than 0 (Figure S6). The FT EXAFS analysis also shows a clear peak corresponding to Bi−O bonds, together with Bi−Bi bonds similar to that observed for the Bimetal reference (Figure S6b,d). Thus, the capacity contribution above 1 V vs Na/Na^+ is attributed to the oxidation of Bi, which was also shown by Surendran et al. through *operando* XAS measurements.[14] This oxidation of Bi can be explained by Bi−O bonds at the interface between the Bi particles and the Na−Fe−O matrix. The contribution from the Bi−O bonds will be significant as long as the Bi particles are relatively small (<10 nm) so that the surface-to-volume ratio is large. In the region where Bi has a positive oxidation state, the main diffraction peak of Bi seems to shift slightly toward higher Q values during desodiation and back again during sodiation (Figure 1d). At this point, we are not able to explain this phenomenon.

There are no signs of the Na−Fe−O matrix in the *operando* XRD measurements as all of the peaks in the XRD pattern can be assigned to the alloying particles (Na_xBi phases) and the Na metal used as a counter electrode. The *operando* XAS study of Surendran et al. showed that Fe was redox active and contributed some to the capacity during the electrochemical cycling of $BiFeO_3$.[14] However, there are no clear plateaus in the (de)sodiation curves in our measurements that should correspond to the reduction or oxidation of Fe. Given the amorphous nature of the Fe-containing phase(s), it would likely exhibit a very gradual redox reaction that is difficult to observe in the (de)sodiation processes dominated by the electrochemistry of Bi. Our ex situ X-ray absorption near edge spectroscopy (XANES) measurements on cycled samples showed a shift in the edge position of Fe proving that it is electrochemically active (Figure S7), even though it is to a smaller extent than what Surendran et al. showed in their *operando* measurement.[14] The apparent differences between Surendran's and our results could originate from different morphologies of the particles and/or inherent differences between ex situ vs *operando* measurements. The XANES data also indicate a significant change in local coordination around the Fe atoms, where a pre-edge peak appears during the first sodiation (Figure S7a). This pre-edge feature is characteristic of tetrahedral coordination of Fe, similar to that in Fe_3O_4, as opposed to the octahedrally coordinated Fe in $BiFeO_3$ that shows no significant pre-edge feature (Figure S7a). Apart from this small change in oxidation state and coordination of Fe, it is difficult to assess the Fe-containing phase(s). However, these results still suggest a dynamic nature of the Na−Fe−O matrix, which might be responsible for the degradation of the material.

Material Degradation. To further understand the degradation processes in $BiFeO_3$, we performed *operando* XRD for 27 cycles between 0.01 and 2.00 V in a half-cell configuration using Na foil as a counter electrode (Figure S8). Since $BiFeO_3$ has the same cycling mechanism at different current densities, a current density of 0.2 A g^{-1} was selected to obtain a good compromise between total measurement time, time resolution, and data quality. Detailed analysis of the *operando* XRD data was combined with ex situ XAS measurements of the Bi L3 edge (Figures 2 and S9, SI). Based on the behavior of $BiFeO_3$, the degradation mechanism could be divided into 3 well-defined regions, where each region is characterized by one specific redox reaction that determines the capacity decay.

Region 1 corresponds to the first 6 cycles and is assigned based on the disappearance of the oxidation of Bi (region 1 in Figure 2a,b). The XAS data from samples extracted after the first and fifth desodiation supports the statement that the capacity decay in this region is due to disappearance of Bi−O bonds at the interface between the Bi particles and the Na−Fe−O matrix (Figure 2c,d). All desodiated samples show characteristic signals for Bi−Bi bonds between 2 and 3.4 Å in the FT EXAFS graphs, indicating the presence of Bi metal (Figure 2d). At the same time, the position of the Bi XANES edge after first desodiation is between the position of Bi metal (Bi^0) and $BiFeO_3$ (Bi^{3+}), meaning that Bi in this sample has a positive average oxidation state roughly between 1 and 2 (Figure 2c). Furthermore, there are clear signals in the FT EXAFS graphs of Bi−O bonds after the first desodiation between the R values of 1 and 2 Å, which mostly disappear

https://doi.org/10.1021/acsami.3c17296
ACS Appl. Mater. Interfaces 2024, 16, 12428−12436

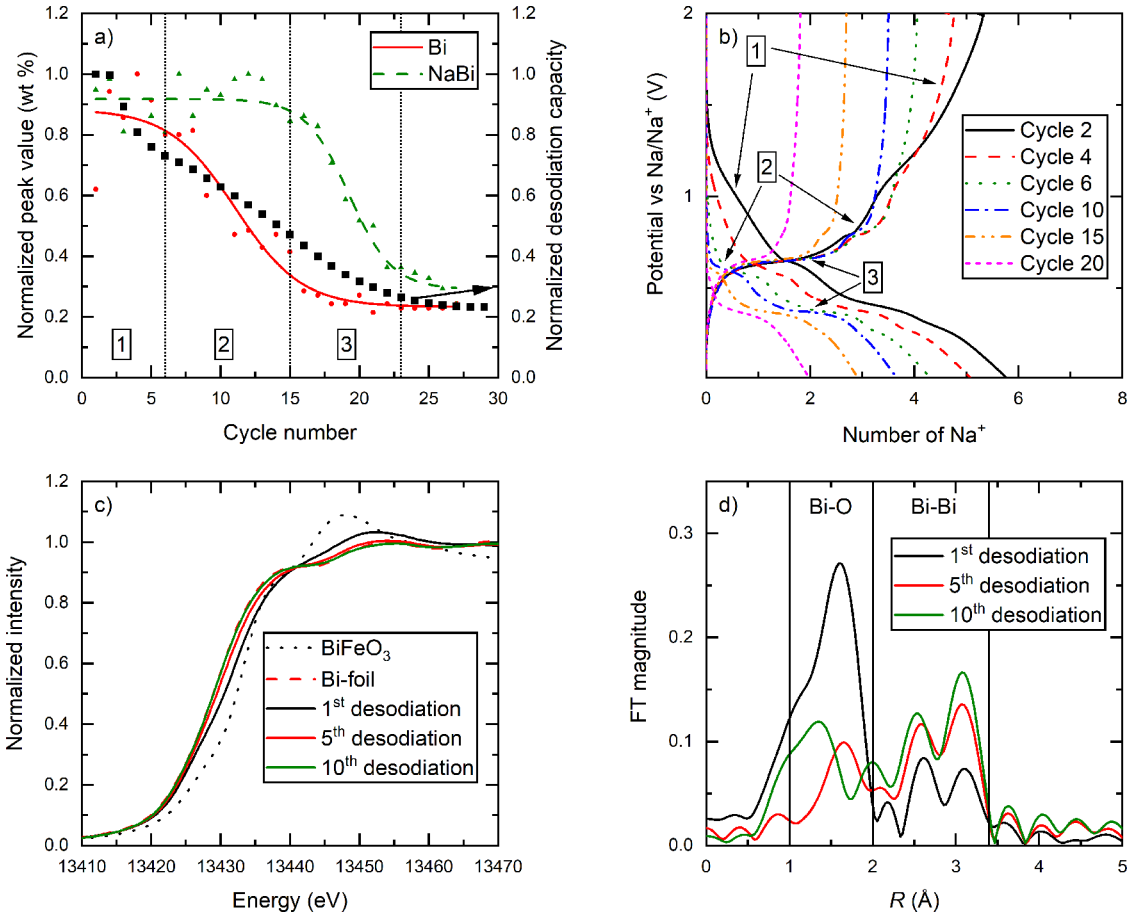

Figure 2. (a) Maximum normalized phase fractions for Bi and NaBi vs cycle number extracted from surface Rietveld refinement on *operando* XRD of $BiFeO_3$ for the first 27 (de)sodiation cycles performed with a specific current of 0.2 A g^{-1} and a voltage range of 0.01−2.00 V vs Na/Na^+. (b) Selected (de)sodiation curves plotted as potential vs Na/Na^+ against the calculated number of Na^+ ions transferred per formula unit obtained from the *operando* measurements shown in (a) highlighting the capacity decay between cycles 2 and 20. (c) XANES spectra of the Bi L3 edge for desodiated $BiFeO_3$ at different stages of cycling compared to pristine $BiFeO_3$ and Bi metal as references. (d) Corresponding FT EXAFS spectra showing the changes in Bi−O bonds.

after the fifth desodiation likely due to coalescence of Bi leading to larger particles inside the Na−Fe−O matrix. The analysis of the diffraction patterns in the fully desodiated state reveals that the diffraction peaks corresponding to the Na_xBi alloys become more pronounced as cycling progresses, confirming an increase of crystallite size (Figure S8, SI). This provides a rationale for the disappearance of the oxidation reaction as bigger particles will have a smaller surface-to-volume ratio and, therefore, fewer Bi−O bonds.

Between cycles 6 and 15 (region 2) the diffraction peaks of Bi gradually disappear together with the (de)sodiation plateaus corresponding to the Bi ⇋ NaBi reaction (Figure 2a,b). The same was observed for Bi_2MoO_6 between cycles 4 and 9 (Figure S10, SI).[22] From cycles 15−26 for $BiFeO_3$ (Figure 2a,b) and cycles 9−13 for Bi_2MoO_6 (Figure S10, SI), the intensities of the NaBi peaks are also greatly reduced, indicating that the NaBi ⇋ Na_3Bi alloying reaction becomes partially irreversible and that the system locks itself in the sodiated state (region 3). Following this, the capacity stabilizes at ∼20% of its initial desodiation capacity, and the main capacity contribution comes from some redox activity between NaBi and Na_3Bi.

Regions 1−3, described above, separate the capacity degradation according to the key chemical processes determining the capacity fading, with the main trigger being growth of the alloying particles inside the Na−Fe−O matrix. This increase in the particle size is most likely driven by the electrochemical sintering of the Na_xBi particles. In the pursuit of the origin of the capacity degradation, we reduced the upper cutoff voltage to 0.7 V vs Na/Na^+ to cycle the material only between NaBi and Na_3Bi using a current density of 0.1 A g^{-1} (Figure 3a,c). This new cutoff voltage limited the reversible capacity to a maximum of ∼230 mAh g^{-1} but increased the cycling stability significantly as the capacity was only reduced to ∼140 mAh g^{-1} after 100 cycles. The performance at a high rate (1 A g^{-1}) was also well maintained (Figure 3b,c). This performance is still not sufficient to be of commercial interest; however, it demonstrates that the electrochemical isolation of the NaBi ⇋ Na_3Bi reaction leads to stable cycling. Galvanostatic cycling up to 0.90 V vs Na/Na^+ was also performed but showed similar capacity fading as during cycling to 2.00 V vs Na/Na^+ (Figure S11). This showed that the Bi ⇋ NaBi reaction and the oxidation of Bi are the main contributors to capacity degradation.

The exact reason the capacity from the Bi ⇋ NaBi reaction and the surface oxidation of Bi decay so quickly is difficult to know with certainty, but it is likely that the large structural changes occurring during cycling are involved. The large volume expansion of ∼250% for the Bi ⇋ h-Na_3Bi reaction could lead to particle cracking, which is potentially the main

https://doi.org/10.1021/acsami.3c17296
ACS Appl. Mater. Interfaces 2024, 16, 12428−12436

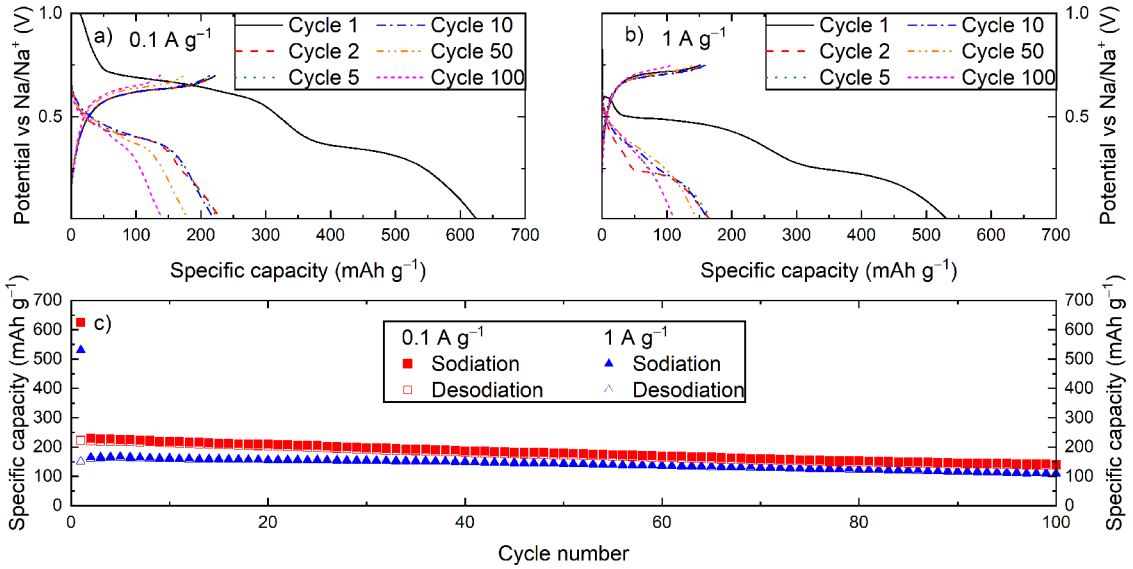

Figure 3. Selected (de)sodiation curves of $BiFeO_3$ cycled at (a) 0.1 A g^{-1} with a voltage range of 0.01−0.70 V vs Na/Na^+ and (b) 1 A g^{-1} with a voltage range of 0.01−0.75 V. (c) Specific (de)sodiation capacity per cycle derived from the measurements in (a) and (b).

reason for the poor cycling stability of pure Bi metal.[24,31] The Na−Fe−O matrix surrounding the Bi nanoparticles formed during the conversion reaction should mitigate some of these problems, but the growth of the alloying particles and the structural changes of the matrix including redox activity on Fe still lead to limited cycling stability. It may be that the matrix and the alloying particles are stable when cycling between NaBi and Na_3Bi but that the transition between Bi and NaBi leads to significant movements in the matrix allowing the alloying particles to coalesce and induce capacity degradation. A more detailed understanding of the structural changes in the matrix and the growth of the Bi particles, especially above 0.7 V vs Na/Na^+, could provide the knowledge needed to stabilize the full two-step (de)alloying reaction to reach an acceptable specific capacity. Finding a material that forms a stable matrix, which can keep the Bi particles in place while still allowing the alloying reactions to occur, will probably be the recipe for a CAM anode with good cycling stability.

CONCLUSIONS

Using *operando* XRD, both at high rates and over 27 (de)sodiation cycles, we have revealed some new insights into the cycling mechanism of $BiFeO_3$. The results reveal that the general cycling mechanism is the same at 1 and 0.1 A g^{-1}. The first sodiation shows an irreversible conversion reaction, forming Bi nanoparticles embedded in a Na−Fe−O matrix. During the following cycles, the main contributor to the capacity is the two-staged alloying mechanisms going from Bi to NaBi and Na_3Bi. We observe both the hexagonal and cubic versions of Na_3Bi, where c-Na_3Bi forms before h-Na_3Bi during sodiation. There is also a significant capacity contribution above 1 V vs Na/Na^+ during desodiation, attributed to the oxidation of the Bi nanoparticles, resulting in Bi−O bonds on the interface toward the Na−Fe−O matrix. This contribution gradually disappears during the first 6 cycles. The following capacity decay is explained by the increasing irreversibility of the alloying reactions where the equilibrium is shifted toward the sodiated phases. Especially for the Bi ⇋ NaBi reaction, which disappears completely. When reducing the upper cutoff voltage to isolate the NaBi ⇋ Na_3Bi reaction, the cycling stability was significantly improved and the high-rate performance was maintained, showing that this reaction in itself is stable. There is still not much knowledge of the Na−Fe−O matrix, but ex situ XAS showed that Fe is electrochemically active and contributes a bit to the capacity. More detailed structural studies are needed to fully understand the nature of the Na−Fe−O matrix and the movement and growth of the Bi particles. This will hopefully enable us to design CAMs with good cycling stability, combined with the already established benefits of high capacity and good rate capabilities.

EXPERIMENTAL SECTION

Synthesis. $BiFeO_3$ was synthesized by a sol−gel method based on the study of Ma et al.,[32] where 1.2 × 10^{-2} mol (5.822 g) $Bi(NO_3)$ ×$5H_2O$ (98%, Sigma-Aldrich) and 1.0 × 10^{-2} mol (4.040 g) $Fe(NO_3)_3$ × $9H_2O$ (≥98%, Sigma-Aldrich) were mixed with 8−10 mL of ethylene glycol (99.8%, Sigma-Aldrich) under magnetic stirring at 100 rpm and 60 °C for 1 h. Subsequently, the temperature was increased to 100 °C to allow for a slow evaporation of the solvent via autocombustion. The resulting dry gel was then transferred to an Al_2O_3 crucible and calcined in air at 350 °C for 3 h in a muffle oven (Carbolite Furnaces CWF 1200) and cooled to room temperature. The product was then crushed to powder in an agate mortar, pressed to a pellet, and treated at 650 °C for 8 h. To decrease the particle size, 2 g of the obtained product was ball-milled with 85 g of 3 mm stainless steel balls in a Pulverisette 7 Premium Line (Fritsch) for 20 min at 250 rpm in an argon atmosphere.

Material Characterization. The XRD samples were prepared by mixing the obtained product with isopropanol (≥99.7%, VWR) and dispersing it on a flat glass plate mounted on the sample holder. All XRD patterns of uncycled samples were collected using a D8 Discover diffractometer (Bruker, Cu-source, λ = 1.5406 Å) with a point detector and fluorescence correction in the 2θ range 10−100° (Q = 0.71−6.25 $Å^{-1}$). One scan lasted ∼3 h. The morphology of the $BiFeO_3$ particles was investigated with a high-resolution Hitachi SU8230 cold-field emission scanning electron microscope operated with an acceleration voltage of 5 kV. The images were generated by secondary electrons, with a working distance of 8.8 mm and magnifications ranging from 1000 to 25,000. The powder was spread out on carbon tape, attached to the sample holder, to fix the powder and ensure good conductivity.

Electrode Preparation. The battery electrodes were made by combining the active material ($BiFeO_3$), binder (carboxymethylcellu-

https://doi.org/10.1021/acsami.3c17296
ACS Appl. Mater. Interfaces 2024, 16, 12428−12436

lose sodium salt, CMC, Sigma-Aldrich), conductive agent (Carbon black, Super P, Timcal), and solvent (distilled H_2O) in an 8:1:1 ratio into a slurry in a Thinky mixer (ARE 250). The mixing procedure consisted of 5 min of mixing at a speed of 2000 rpm, followed by a defoaming step for 1.5 min at 750 rpm. After the mixing procedure, which was repeated if necessary, the slurry was coated onto a dendritic Cu foil (Schlenk, 10 μm thick) with a coating height of 300 μm. The resulting electrode sheets were dried in air overnight, cut into 15 mm discs the following day, and were further dried in a Büchi oven at 60 °C under dynamic vacuum for 3 h. Afterward, the electrodes were placed into a glovebox (MBraun Labmaster, H_2O and O_2 < 0.1 ppm) for coin cell assembly.

Electrochemical Characterization. Electrochemical characterization was performed in half-cells with metallic Na as the counter electrode. Na chunks (Sigma-Aldrich) were cut into smaller pieces, rolled flat, and then stamped into 14 mm discs. The discs were then brushed on each side with a toothbrush (medium, First Price) to ensure a fresh surface. Each Na disc was placed in a coin cell (CR2032, stainless steel, 304, Pi-Kem) together with a separator (Whatman GE, 16 mm) and wetted with 80 μL of electrolyte and the working electrode before the battery was closed using an automatic coin cell crimper (Hohsen). The electrolyte was mixed inside the glovebox and consisted of 1 M $NaPF_6$ (Fluorochem) in propylene carbonate (PC, 99.7%, Sigma-Aldrich) with 5% fluoroethylene carbonate (FEC, 99%, Sigma-Aldrich) as an additive.

Galvanostatic cycling (GC) of the batteries was carried out with a Neware battery tester (CT-4008T-5V10mA-164) at 25 °C with a lower cutoff voltage of 0.01 V and current densities of 0.1 and 1 A g^{-1} with respect to the mass of $BiFeO_3$. The active mass loading of the electrodes was between 1 and 2 mg cm^{-2}. The upper cutoff voltage was 2 V for most of the measurements, but it was reduced to 0.7 V for one measurement at 0.1 A g^{-1} and to 0.75 at 1 A g^{-1} in order to isolate the NaBi ⇋ Na_3Bi reaction. The higher upper cutoff voltage for the 1 A g^{-1} measurement was chosen to account for the increased overpotential at higher current densities. Cyclic voltammetry (CV) measurements were performed with an MPG2 battery cycler (BioLogic) using a voltage window of 0.01−2.00 V and sweep rates of 0.1 and 1 mV s^{-1}.

***Operando* XRD.** Laboratory manufactured *operando* cells similar to the one presented by Drozhzhin et al. with glassy carbon windows were used for the *operando* XRD measurements.[33] The electrode for the *operando* measurement over the course of 2 (de)sodiation cycles at 0.1 A g^{-1} was made by drop-casting the slurry directly onto one of the cell halves to optimize the XRD signals. The measurement over 27 cycles used normal electrodes on Cu foil to ensure good electrochemical performance. Apart from this, the assembly was performed as similar as possible to the normal coin cells. The GC measurements of these two *operando* measurements were performed using an SP150 battery cycler (BioLogic) with a voltage range of 0.01−2.00 V and current densities of 0.1 A g^{-1} (2 cycles) and 0.2 A g^{-1} (27 cycles). The XRD measurements were performed simultaneously with continuous still scans (10 min $scan^{-1}$, Q = 1.26−3.65 $Å^{-1}$) using a Dectris Eiger2 R 500 K detector on a Bruker D8 Advance diffractometer (Mo source, $\lambda_{k\alpha1}$ = 0.7093 Å, $\lambda_{k\alpha2}$ = 0.7136 Å, focusing mirror primary optic).

The high-rate *operando* XRD measurement with a current density of 1 A g^{-1} and a voltage range of 0.01−2.00 V was also performed over the course of 2 cycles. This measurement was performed with synchrotron radiation at BM31, which is a part of the Swiss-Norwegian Beamlines (SNBL), at ESRF with a wavelength of 0.24486 Å and a Pilatus CdTe 2 M detector from DECTRIS. Each scan had an exposure time of 20 s with 15 repetitions that was averaged, giving a total measurement time of 5 min per data point. The electrode used for this measurement was coated with a wet thickness of 500 μm on a Cu foil.

Ex Situ XAS. Electrodes for ex situ XAS were prepared in the same way as that for normal coin cells. The batteries were cycled at 0.1 A g^{-1} between 0.01 and 2.00 V until the desired stage of cycling (specified in main text) where they then went through a constant voltage step where the cutoff voltage was held until the current was below 20 μA. The coin cells were then transferred to the glovebox and disassembled with a coin cell disassembling tool (Hoshen). The electrodes were carefully extracted from the disassembled coin cells, cleaned with ∼0.5 mL of DEC per electrode, and dried for 1 h inside the glovebox. Following this, the electrode material was scraped from the Cu foil, ground carefully in a mortar, and filled in 1 mm borosilicate glass capillaries that were sealed with UV glue (Bondic). The XAS measurements on the Bi L3 edge were performed in transmission mode with ion chamber detectors in the energy range of 13.32−14.10 keV, 0.7 eV step size, and 200 ms exposure giving a measurement time of 3 min and 44 s per scan. Each sample was measured with 2 repetitions, which were averaged in Athena.[34] The Fe K edge was measured in fluorescence mode with an energy range of 7.05−7.26 keV, 0.3 eV step size, and 200 ms exposure, leading to a total measurement time of 2 min and 20 s.

Software and Data Treatment. To visualize the crystal structure of $BiFeO_3$, we utilized Vesta.[35,36] J-edit and Topas v6[37] were used for Rietveld refinements, while EC-lab and software from Neware were used to process electrochemistry data. Python 3 and Origin 2020 were utilized for further processing and plotting of the data, including python scripts provided by the BM31 staff. The Athena software was used for processing and analyzing the XAS data.[34]

■ ASSOCIATED CONTENT

Data Availability Statement

All the background data for this publication including procedures and scripts for data treatment are available at dataverse.no.[38] Additional data and analysis from the $BiFeO_3$ system are also available.[39]

Supporting Information

The Supporting Information is available free of charge at https://pubs.acs.org/doi/10.1021/acsami.3c17296.

XRD and SEM data of pristine $BiFeO_3$; (de)sodiation curves and cycling voltammograms at different cycling conditions; ex situ XRD and XAS data from cycled $BiFeO_3$ samples; contour plot from *operando* XRD of $BiFeO_3$ over 27 cycles with corresponding dQ/dV curves; and results from surface Rietveld refinement of *operando* XRD of Bi_2MoO_6 (PDF)

■ AUTHOR INFORMATION

Corresponding Authors

Anders Brennhagen − *Centre for Materials Science and Nanotechnology, Department of Chemistry, University of Oslo, N-0315 Oslo, Norway;* orcid.org/0000-0003-4467-6750; Email: anders.brennhagen@smn.uio.no

Helmer Fjellvåg − *Centre for Materials Science and Nanotechnology, Department of Chemistry, University of Oslo, N-0315 Oslo, Norway*; Email: helmer.fjellvag@kjemi.uio.no

Authors

Casper Skautvedt − *Centre for Materials Science and Nanotechnology, Department of Chemistry, University of Oslo, N-0315 Oslo, Norway;* orcid.org/0000-0002-4521-3080

Carmen Cavallo − *CENATE, Centrifugal Nanotechnology, 1814 Askim, Norway;* orcid.org/0000-0003-1931-3018

David S. Wragg − *Centre for Materials Science and Nanotechnology, Department of Chemistry, University of Oslo, N-0315 Oslo, Norway; Department of Battery Technology, Institute for Energy Technology (IFE), 2007 Kjeller, Norway;* orcid.org/0000-0001-8502-7912

https://doi.org/10.1021/acsami.3c17296
ACS Appl. Mater. Interfaces 2024, 16, 12428−12436

Alexey Y. Koposov − *Centre for Materials Science and Nanotechnology, Department of Chemistry, University of Oslo, N-0315 Oslo, Norway; Department of Battery Technology, Institute for Energy Technology (IFE), 2007 Kjeller, Norway;* orcid.org/0000-0001-5898-3204

Anja O. Sjåstad − *Centre for Materials Science and Nanotechnology, Department of Chemistry, University of Oslo, N-0315 Oslo, Norway*

Complete contact information is available at: https://pubs.acs.org/10.1021/acsami.3c17296

Funding

Norges Forskningsråd (The Research Council of Norway, NFR) through NanoName: improving sodium ion battery performance with nanostructured metalate anodes (Project number: 287480) and RECX (Norwegian National Resource Centre for X-ray Diffraction and Scattering) for usage of X-ray radiation facilities (Funded by NFR, project number: 208896).

Notes

The authors declare no competing financial interest.

■ ACKNOWLEDGMENTS

Salah Bra Amedi is acknowledged for assisting in the synthesis of $BiFeO_3$. The Swiss Norwegian beamlines (SNBL, ESRF) are acknowledged for provision of beamtime and its staff for invaluable support. The BM31 setup was funded by the Swiss National Science Foundation (grant 206021_189629) and the Research Council of Norway.

■ ABBREVIATIONS

CAM, conversion-alloying material
CMC, carboxymethylcellulose sodium salt
CV, cyclic voltammetry
ESRF, European Synchrotron Radiation Facility
EXAFS, extended X-ray absorption fine structure
FEC, fluoroethylene carbonate
FT, Fourier transform
GC, galvanostatic cycling
LIB, Li-ion battery
NIB, Na-ion battery
NFR, Norges Forskningsråd (The Research Council of Norway)
PC, propylene carbonate
RECX, Resource Centre for X-ray Diffraction and Scattering
SEM, scanning electron microscopy
SEI, solid electrolyte interface
SNBL, Swiss-Norwegian beamlines
TSCT, total scattering computed tomography
TEM, transition electron microscopy
TM, transition metal
XANES, X-ray absorption near edge spectroscopy
XAS, X-ray absorption spectroscopy
XRD, X-ray diffraction

■ REFERENCES

(1) Vaalma, C.; Buchholz, D.; Weil, M.; Passerini, S. A Cost and Resource Analysis of Sodium-Ion Batteries. *Nat. Rev. Mater.* **2018**, *3* (4), 18013.

(2) Hasa, I.; Mariyappan, S.; Saurel, D.; Adelhelm, P.; Koposov, A. Y.; Masquelier, C.; Croguennec, L.; Casas-Cabanas, M. Challenges of Today for Na-Based Batteries of the Future: From Materials to Cell Metrics. *J. Power Sources* **2021**, *482*, No. 228872.

(3) Mukherjee, S.; Bin Mujib, S.; Soares, D.; Singh, G. Electrode Materials for High-Performance Sodium-Ion Batteries. *Materials* **2019**, *12* (12), 1952.

(4) Chayambuka, K.; Mulder, G.; Danilov, D. L.; Notten, P. H. From Li-Ion Batteries toward Na-Ion Chemistries: Challenges and Opportunities. *Adv. Energy Mater.* **2020**, *10* (38), No. 2001310.

(5) Zhang, H.; Hasa, I.; Passerini, S. Beyond Insertion for Na-Ion Batteries: Nanostructured Alloying and Conversion Anode Materials. *Adv. Energy Mater.* **2018**, *8* (17), No. 1702582.

(6) Skurtveit, A.; Brennhagen, A.; Park, H.; Cavallo, C.; Koposov, A. Benefits and Development Challenges for Conversion-Alloying Anode Materials for Na-Ion Batteries. *Front. Energy Res.* **2022**, *10*, No. 897755, DOI: 10.3389/fenrg.2022.897755.

(7) Fang, L.; Bahlawane, N.; Sun, W.; Pan, H.; Xu, B. B.; Yan, M.; Jiang, Y. Conversion-Alloying Anode Materials for Sodium Ion Batteries. *Small* **2021**, *17* (37), No. 2101137.

(8) Liu, D.; Shadike, Z.; Lin, R.; Qian, K.; Li, H.; Li, K.; Wang, S.; Yu, Q.; Liu, M.; Ganapathy, S. Review of Recent Development of In Situ/Operando Characterization Techniques for Lithium Battery Research. *Adv. Mater.* **2019**, *31* (28), No. 1806620.

(9) Brennhagen, A.; Cavallo, C.; Wragg, D. S.; Sottmann, J.; Koposov, A. Y.; Fjellvåg, H. Understanding the (De)Sodiation Mechanisms in Na-Based Batteries through Operando X-Ray Methods. *Batteries & Supercaps* **2021**, *4* (7), 1039−1063.

(10) Gao, H.; Ma, W.; Yang, W.; Wang, J.; Niu, J.; Luo, F.; Peng, Z.; Zhang, Z. Sodium Storage Mechanisms of Bismuth in Sodium Ion Batteries: An Operando X-Ray Diffraction Study. *J. Power Sources* **2018**, *379*, 1−9.

(11) Sottmann, J.; Homs-Regojo, R.; Wragg, D. S.; Fjellvåg, H.; Margadonna, S.; Emerich, H. Versatile Electrochemical Cell for Li/Na-Ion Batteries and High-Throughput Setup for Combined Operando X-Ray Diffraction and Absorption Spectroscopy. *J. Appl. Crystallogr.* **2016**, *49* (6), 1972−1981.

(12) Ou, X.; Yang, C.; Xiong, X.; Zheng, F.; Pan, Q.; Jin, C.; Liu, M.; Huang, K. A New Rgo-Overcoated Sb_2Se_3 Nanorods Anode for Na^+ Battery: In Situ X-Ray Diffraction Study on a Live Sodiation/Desodiation Process. *Adv. Funct. Mater.* **2017**, *27* (13), No. 1606242.

(13) Ruud, A.; Sottmann, J.; Vajeeston, P.; Fjellvåg, H. Operando Investigations of Lithiation and Delithiation Processes in a $BiVO_4$ Anode Material. *Phys. Chem. Chem. Phys.* **2018**, *20* (47), 29798−29803.

(14) Surendran, A.; Enale, H.; Thottungal, A.; Sarapulova, A.; Knapp, M.; Nishanthi, S.; Dixon, D.; Bhaskar, A. Unveiling the Electrochemical Mechanism of High-Capacity Negative Electrode Model-System $BiFeO_3$ in Sodium-Ion Batteries: An in Operando XAS Investigation. *ACS Appl. Mater. Interfaces* **2022**, *14* (6), 7856−7868.

(15) Sottmann, J.; Ruud, A.; Fjellvåg, Ø. S.; Vaughan, G. B. M.; Di Michel, M.; Fjellvåg, H.; Lebedev, O. I.; Vajeeston, P.; Wragg, D. S. 5D Total Scattering Computed Tomography Reveals the Full Reaction Mechanism of a Bismuth Vanadate Lithium Ion Battery Anode. *Phys. Chem. Chem. Phys.* **2022**, *24* (44), 27075−27085.

(16) Dixon, D.; Ávila, M.; Ehrenberg, H.; Bhaskar, A. Difference in Electrochemical Mechanism of SnO2 Conversion in Lithium-Ion and Sodium-Ion Batteries: Combined in Operando and Ex Situ XAS Investigations. *ACS Omega* **2019**, *4* (6), 9731−9738.

(17) Kim, Y.; Kim, Y.; Choi, A.; Woo, S.; Mok, D.; Choi, N.-S.; Jung, Y. S.; Ryu, J. H.; Oh, S. M.; Lee, K. T. Tin Phosphide as a Promising Anode Material for Na-Ion Batteries. *Adv. Mater.* **2014**, *26* (24), 4139−4144.

(18) Wu, Y.; Luo, W.; Gao, P.; Zhu, C.; Hu, X.; Qu, K.; Chen, J.; Wang, Y.; Sun, L.; Mai, L.; Xu, F. Unveiling the Microscopic Origin of Asymmetric Phase Transformations in (De)Sodiated Sb_2Se_3 with in Situ Transmission Electron Microscopy. *Nano Energy* **2020**, *77*, No. 105299.

(19) Ma, C.; Xu, J.; Alvarado, J.; Qu, B.; Somerville, J.; Lee, J. Y.; Meng, Y. S. Investigating the Energy Storage Mechanism of SnS_2-RGO Composite Anode for Advanced Na-Ion Batteries. *Chem. Mater.* **2015**, *27* (16), 5633−5640.

(20) Sottmann, J.; Herrmann, M.; Vajeeston, P.; Ruud, A.; Drathen, C.; Emerich, H.; Wragg, D. S.; Fjellvåg, H. Bismuth Vanadate and Molybdate: Stable Alloying Anodes for Sodium-Ion Batteries. *Chem. Mater.* **2017**, *29* (7), 2803−2810.
(21) Ruud, A.; Sottmann, J.; Vajeeston, P.; Fjellvåg, H. Direct Observation of Reversible Conversion and Alloying Reactions in a $Bi_2(MoO_4)_3$-Based Lithium-Ion Battery Anode. *Journal of Materials Chemistry A* **2019**, *7* (30), 17906−17913.
(22) Brennhagen, A.; Cavallo, C.; Wragg, D. S.; Vajeeston, P.; Sjåstad, A. O.; Koposov, A. Y.; Fjellvåg, H. Operando XRD Studies on Bi_2MoO_6 as Anode Material for Na-Ion Batteries. *Nanotechnology* **2022**, *33* (18), 185402.
(23) Xu, X.; Li, M.; Yu, T. Facile Synthesis of Bi_2MoO_6 Nanosheets@ Nitrogen and Sulfur Codoped Graphene Composites for Sodium-Ion Batteries. *Chemical Research in Chinese Universities* **2020**, *36* (1), 115−119.
(24) Sottmann, J.; Herrmann, M.; Vajeeston, P.; Hu, Y.; Ruud, A.; Drathen, C.; Emerich, H.; Fjellvag, H.; Wragg, D. S. How Crystallite Size Controls the Reaction Path in Nonaqueous Metal Ion Batteries: The Example of Sodium Bismuth Alloying. *Chem. Mater.* **2016**, *28* (8), 2750−2756.
(25) Durai, L.; Moorthy, B.; Thomas, C. I.; Kim, D. K.; Bharathi, K. K. Electrochemical Properties of $BiFeO_3$ Nanoparticles: Anode Material for Sodium-Ion Battery Application. *Mater. Sci. Semicond. Process.* **2017**, *68*, 165−171.
(26) Zhang, X.; van Hulzen, M.; Singh, D. P.; Brownrigg, A.; Wright, J. P.; van Dijk, N. H.; Wagemaker, M. Direct View on the Phase Evolution in Individual $LiFePO_4$ Nanoparticles During Li-Ion Battery Cycling. *Nat. Commun.* **2015**, *6* (1), 8333.
(27) Liu, H.; Strobridge, F. C.; Borkiewicz, O. J.; Wiaderek, K. M.; Chapman, K. W.; Chupas, P. J.; Grey, C. P. Capturing Metastable Structures During High-Rate Cycling of $LiFePO_4$ Nanoparticle Electrodes. *Science* **2014**, *344* (6191), No. 1252817.
(28) Kim, M.-K.; Yu, S.-H.; Jin, A.; Kim, J.; Ko, I.-H.; Lee, K.-S.; Mun, J.; Sung, Y.-E. Bismuth Oxide as a High Capacity Anode Material for Sodium-Ion Batteries. *Chem. Commun.* **2016**, *52* (79), 11775−11778.
(29) Lu, X.; Wang, Z.; Liu, K.; Luo, J.; Wang, P.; Niu, C.; Wang, H.; Li, W. Hierarchical Sb_2MoO_6 Microspheres for High-Performance Sodium-Ion Battery Anode. *Energy Storage Materials* **2019**, *17*, 101−110.
(30) Sottmann, J.; Di Michiel, M.; Fjellvåg, H.; Malavasi, L.; Margadonna, S.; Vajeeston, P.; Vaughan, G. B. M.; Wragg, D. S. Chemical Structures of Specific Sodium Ion Battery Components Determined by Operando Pair Distribution Function and X-Ray Diffraction Computed Tomography. *Angew. Chem., Int. Ed.* **2017**, *56* (38), 11385−11389.
(31) Lim, C.-H.; Selvaraj, B.; Song, Y.-F.; Wang, C.-C.; Jin, J.-T.; Huang, S.-S.; Chuang, C.-H.; Sheu, H.-S.; Liao, Y.-F.; Wu, N.-L. Insight into Microstructural and Phase Transformations in Electrochemical Sodiation−Desodiation of a Bismuth Particulate Anode. *Journal of Materials Chemistry A* **2017**, *5* (40), 21536−21541.
(32) Ma, C.-J.; Li, N.; Song, W.-L. Tailoring the Electrochemical Behaviors of Bismuth Ferrite Using Ca Ion Doping. *Front. Mater.* **2020**, *7*, 15.
(33) Drozhzhin, O. A.; Tereshchenko, I. V.; Emerich, H.; Antipov, E. V.; Abakumov, A. M.; Chernyshov, D. An Electrochemical Cell with Sapphire Windows for Operando Synchrotron X-Ray Powder Diffraction and Spectroscopy Studies of High-Power and High-Voltage Electrodes for Metal-Ion Batteries. *Journal of Synchrotron Radiation* **2018**, *25* (2), 468−472.
(34) Ravel, B.; Newville, M. ATHENA, ARTEMIS, HEPHAESTUS: Data Analysis for X-Ray Absorption Spectroscopy Using IFEFFIT. *Journal of Synchrotron Radiation* **2005**, *12* (4), 537−541.
(35) Momma, K.; Izumi, F. Vesta: A Three-Dimensional Visualization System for Electronic and Structural Analysis. *Journal of Applied crystallography* **2008**, *41* (3), 653−658.
(36) Momma, K.; Izumi, F. Vesta 3 for Three-Dimensional Visualization of Crystal, Volumetric and Morphology Data. *Journal of applied crystallography* **2011**, *44* (6), 1272−1276.
(37) Coelho, A. A. Topas and Topas-Academic: An Optimization Program Integrating Computer Algebra and Crystallographic Objects Written in C++. *J. Appl. Crystallogr.* **2018**, *51* (1), 210−218.
(38) Brennhagen, A. Nafuma. *Experimental Data for the Nanoname Project*, DataverseNO, 2023, DOI: 10.18710/ZFADJS.
(39) Skautvedt, C. E. *Syntese og Karakterisering av $BiFeO_3$ Som Anodemateriale i Na-Ionebatterier*, Master thesis; University of Oslo, 2022.

https://doi.org/10.1021/acsami.3c17296
ACS Appl. Mater. Interfaces 2024, 16, 12428−12436